Optimized Design of Passive Array Coils for High-Efficiency and Anti-Misalignment WPT System

Cancan Rong, *Member, IEEE*, Mengmeng Chen, Xiaoyu Duan, Yunhai Liu, Junhao Wu, Yingqin Zeng, Xiangrui He, Zhijuan Liao, and Chenyang Xia, *Member, IEEE*

***Abstract*—Mid-range wireless power transfer (WPT) system for consumer electronics has been hamstrung by modest energy efficiencies and low misalignment tolerance. As the increase in transfer distance, the increasing leakage magnetic flux between transmitting coil and receiving will deteriorate the system performance. In this article, a novel optimization-based design method of passive array coils (PACs) is presented in order to maximize the power transfer efficiency (PTE) and improve the misalignment tolerance in WPT system. A modified multiobjective genetic algorithm is implemented to optimize parameters of PACs in consideration of PTE, displacement flexibility and volume of PACs. Moreover, a parameter design scheme for compensation network, namely Series-Seriess-Series topology for co-planar multiple coils is investigated, which can achieve zero phase angle in primary side and enhance power factor. Finally, the reasonable prototype of the proposed WPT system with PACs is designed, fabricated and tested. The experimental results show that the proposed structure can increase the efficiency by almost 50% over the system without PACs at 400 mm distance and deliver almost 40 W of output power. Moreover, the PTE and output power can still remain stable under large lateral misalignment with PACs.**

***Index Terms*—Misalignment tolerance, modified multiobjective genetic algorithm (GA), passive array coils (PACs), power transfer efficiency (PTE), wireless power transfer (WPT).**

I. Introduction

WIRELESS power transfer (WPT) technology has become a hotspot field and gained widespread attention due to many prominent advantages, such as flexibility, reliability and safety [1], [2], [3], [4]. This surge on interest has been powered by the increasing adoption of: electric cars [1], medical implantable devices [5], [6], Internet of Things (IoTs) [7], etc. WPT system transmit power via leveraging the magnetic field produced by magnetic coupling resonance between transmitter and receiver. In practical, the weak coupling coefficient between coils has been the major constraint for mid-range WPT system [3], [8]. Mutual coupling decays rapidly when the transfer distance increases or the coil misalignment occurs, which could deteriorate the transmission performances of WPT system [8], [9]. Therefore, it is of great significance to improve power transfer efficiency (PTE) and displacement flexibility (DF) of the WPT system.

Up to now, there are several methods reported to improve PTE or DF of mid-range WPT system [8], [9], [10], [11], [12], [13]. Among these researches, it is a promising solution to put repeater between the magnetic coupler, such as metamaterials and passive array coils (PACs). In [14], a thin printed circuit board type hybrid metamaterial slab (operating frequency at 6.78 MHz) was designed to increase efficiency and reduce electromagnetic field simultaneously. The proposed metamaterial showed excellent performance and provided great guidance for later studies [6]. In [15], a metamaterial-coupled WPT system based on cubic high-dielectric resonators was presented ($f_1 = 560$ MHz and $f_2 = 1.7$ GHz), and the metamaterial could increase the transfer distance and provide insight into the mis-alignment tolerant ability. However, the working frequencies of metamaterial-based WPT system are generally high (at least MHz) for better representation of exotic physical properties [3], [4]. Therefore, it is inappropriate for high-power applications since the traditional operational frequency of the power switching device for WPT system is normally at the range of kHz [16]. Correspondingly, repeater at kHz frequency band were proposed to enhance power transfer capability of WPT system. In [17], a hybrid loop array was proposed which could enhance the efficiency and reduce electromagnetic field at the same time. In [18], a 3×3 matrix power repeater was presented to improve the PTE. However, these studies lack detailed repeater optimization processes and make no mention of misalignment tolerance. In addition, the parameters of the compensation network are unmentioned with the constraint of zero phase angle (ZPA) in primary side. Thus, it has been still an unsolved challenge that designs a high efficiency and good misalignment tolerance magnetic coupling structure combined with efficient optimization method in the WPT system.

For the above-mentioned analysis, this article proposes WPT system with PACs for higher PTE and better misalignment tolerance. The magnetic coupling structure is designed and optimized with a comprehensive consideration of transfer performance

Manuscript received 7 November 2023; revised 15 January 2024; accepted 7 February 2024. Date of publication 13 February 2024; date of current version 20 March 2024. This work was supported by the National Natural Science Foundation of China under Grant 52207019. Recommended for publication by Associate Editor X. Ruan. *(Corresponding author: Cancan Rong.)*

Cancan Rong, Mengmeng Chen, Xiaoyu Duan, Yunhai Liu, Junhao Wu, Zhijuan Liao, and Chenyang Xia are with the School of Electrical and Power Engineering, China University of Mining and Technology, Xuzhou 221116, China (e-mail: ccrong@cumt.edu.cn; 17184992@cumt.edu.cn; dichar@cumt.edu.cn; liuyunhai@cumt.edu.cn; 17195484@cumt.edu.cn; zjliao@cumt.edu.cn; chyxia@cumt.edu.cn).

Yingqin Zeng and Xiangrui He are with the School of Electrical and Electronic Engineering, Huazhong University of Science and Technology, Wuhan 430074, China (e-mail: yqzeng@hust.edu.cn; xiangruihe@hust.edu.cn).

Color versions of one or more figures in this article are available at https://doi.org/10.1109/TPEL.2024.3365129.

Digital Object Identifier 10.1109/TPEL.2024.3365129

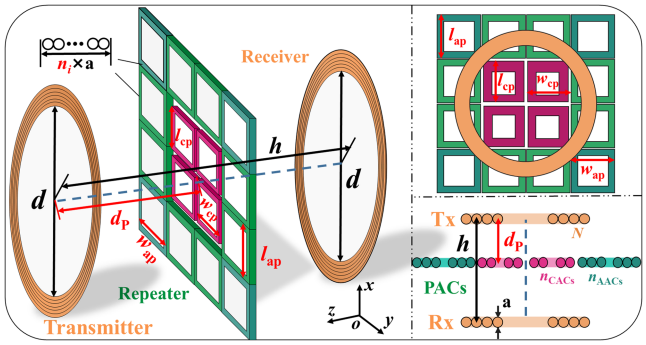

Fig. 1. General overview of the WPT system with PACs.

TABLE I
MAIN PHYSICAL PARAMETERS OF WPT SYSTEM

Symbol	Value	Symbol	Value
d	240 mm	N	10
h	400 mm	f	85 kHz
	a		2.42 mm

and weight. Then, compensation network parameters have been fully studied. Finally, we design and fabricate an experimental prototype to further verify the results. The main contributions of this article are listed as follows.

1) A modified multiobjective genetic algorithm (GA) is implemented to optimize two kinds of PACs' parameters for higher transfer efficiency, better misalignment tolerance, and lower coils volume simultaneously.
2) A novel parameter design scheme of compensation network named Series-Seriess-Series (S-Ss-S) topology for co-planar multiple coils is presented, which can realize ZPA in primary side and increase power factor.

II. MAGNETIC COUPLING STRUCTURE DESIGN

The general overview of the WPT system with PACs in real application is shown in Fig. 1. The proposed system consists of transmitting (*Tx*) coil and receiving (*Rx*) coil, and PACs are placed coaxially between them. Prior to the system theoretical research, the shape of each module in the WPT system should be determined. In general, the circular coils have been adopted for both *Tx* and *Rx* coil to achieve stronger coupling effect under the condition of the given transfer distance [2]. Depending on the nature of the application, the transmission distance h between *Tx* and *Rx* coils is set as 400 mm for mid-range transmission. The diameter d and the turn number N of the two coil resonators is 240 mm and 10, respectively. Fig. 2 compares the coupling coefficient k variation trend with lateral offset distance Δy for circular-circular coil and circular-square coil. It can be found that the coupling effect of circular-square coil is stronger than circular-circular type. In addition, multiple square-type coils are easier to arranged and assembled. Therefore, square spiral coils are employed for the unit cell of the PACs. The operating frequency of the proposed WPT system f is 85 kHz. The inherent parameters of the WPT system are given in Table I. This

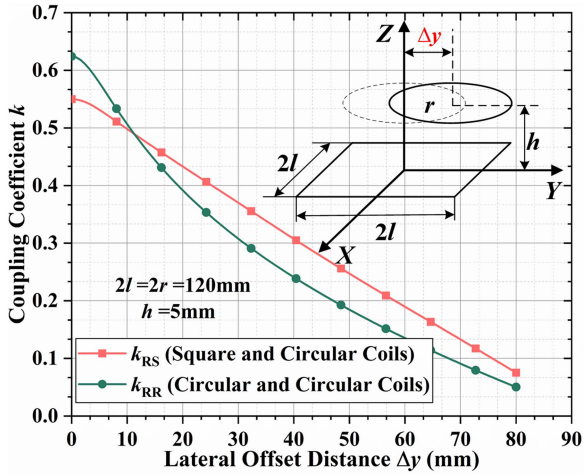

Fig. 2. Coupling properties between different coils.

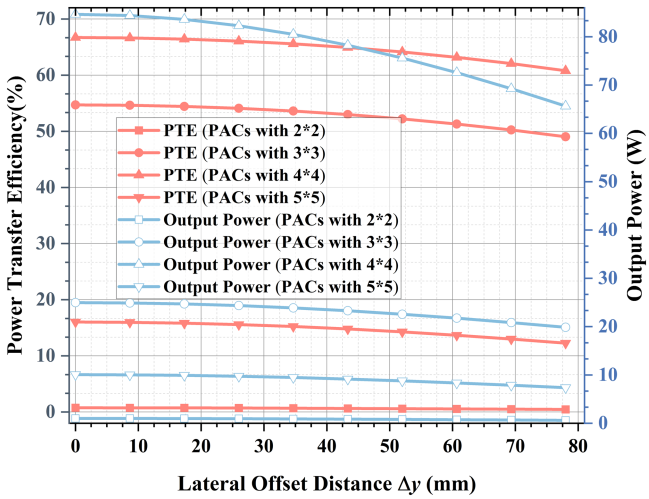

Fig. 3. Analysis and comparison of lateral misalignment of output power and PTE of WPT system with PACs of different array levels.

frequency is widely applied in smart home applications wireless charging and can be easily available [19].

The effect for WPT system with PACs of different array designs on PTE and DF is illustrated by Fig. 3. It can be observed obviously that PTE and DF are not always increase with the number of array unit cells of PACs. This is because the more array unit cells of PACs could result in the additional eddy current losses of PACs. It will cause the precise "focusing" of the PACs for PTE enhancement to be suppressed by the additional eddy current losses. Finally, the 4×4 array design scheme has been employed for better transfer performance after comprehensive tradeoff between PTE and limitation of the actual operating environment.

The proposed PACs are composed of two types of loops: concentrate array coils (CACs) and auxiliary array coils (AACs). It is assumed that the transmitting magnetic flux density $\dot{B}_{T\text{-}P}$

at any point P of magnetic coupling structure is defined as

$$\begin{aligned}\dot{B}_{T\text{-}P} &= B_0 e^{j\beta x_{T\text{-}P}} \cdot \frac{\dot{x}_{T\text{-}P}}{\left|\dot{x}_{T\text{-}P}\right|} \\ &= B_0 e^{j\omega t_{\mathrm{T-P}}} \cdot \frac{\dot{x}_{\mathrm{T-P}}}{\left|\dot{x}_{\mathrm{T-P}}\right|}\end{aligned} \tag{1}$$

where β is the propagation constant of the electromagnetic wave and can be obtained by (2), $\dot{x}_{T\text{-}P}$ is the geometric displacement of the *Tx* coil to the point *P* and ω is operating angular frequency

$$\beta = c\sqrt{\mu_0 \varepsilon} \tag{2}$$

where c is speed of propagation of light, μ_0 is the vacuum permeability, and ε is the vacuum conductivity.

The induced current of PACs I_i (i = the number of CACs and AACs) can be obtained by (3) based on Faraday's law

$$\begin{aligned}I_{\mathrm{i}} &= -\frac{d\Psi}{Z_{\mathrm{i}} dt} = -\frac{\dot{S}_{\mathrm{cell}} \cdot d\dot{B}_{\mathrm{T-cell}}}{Z_{\mathrm{i}} dt} = \frac{\dot{S}_{\mathrm{cell}} \cdot d\dot{B}_{\mathrm{T-cell}}}{R_{\mathrm{i}} + j\omega L_{\mathrm{i}} + \frac{1}{j\omega C_{\mathrm{i}}}} \\ &= \frac{\dot{S}_{\mathrm{cell}} \cdot d\dot{B}_{T-\mathrm{cell}}}{R_i + j\omega L_i - j\frac{\omega_i^2 \cdot L_i}{\omega}} = \frac{\dot{S}_{\mathrm{cell}} \cdot d\dot{B}_{T-\mathrm{cell}}}{R_i + j\frac{(\omega^2 - \omega_i^2) L_i}{\omega} dt} \\ &\approx -\frac{f^2 B_0 \left|\dot{S}_{\mathrm{cell}}\right|}{(f^2 - {f_i}^2) L_i} e^{j\omega t_{T\text{-}P}} \cdot \cos\left\langle \dot{S}_{\mathrm{cell}}, d\dot{B}_{T-\mathrm{cell}} \right\rangle\end{aligned} \tag{3}$$

where Z_i denotes the impedance of the unit cell of PACs at the operating frequency.

Then, the magnetic flux density of PACs unit cell $\dot{B}_{\text{cell-}P}$ at point P could be derived by using (1)–(4). It can be seen that the incoming magnetic field could be regulated by designing inductance L_i, resonant frequency f_i of AACs and CACs, respectively,

$$\dot{B}_{\text{cell-}P} = \frac{\mu_0}{4\pi} \int_L \frac{I_i}{{x_{\text{cell-}P}}^3} d\dot{l} \times \dot{x}_{\text{cell-}P} \tag{4}$$

where $\dot{x}_{\text{cell-}P}$ is the geometric displacement of the unit cell to the point *P*.

Finally, the induced voltages of the *Tx* coil $V_{T\text{-}P}$ at point *P* could be calculated as

$$\begin{aligned}V_{T\text{-}P} &= -\frac{d\Psi}{dt} = -\frac{\dot{S}_P \cdot d\dot{B}_{T\text{-}P}}{dt} \\ &= -j\omega B_0 \left|\dot{S}_P\right| e^{j\omega t_{T\text{-}P}} \cdot \cos\left\langle \dot{S}_P, d\dot{B}_{T\text{-}P} \right\rangle.\end{aligned} \tag{5}$$

The induced voltages of the unit cell $V_{\text{cell-}P}$ at point *P* could be calculated as

$$\begin{aligned}V_{\mathrm{cell\text{-}P}} &= -\frac{d\Psi}{dt} = -\frac{\dot{S}_{\mathrm{P}} \cdot d\dot{B}_{\mathrm{cell\text{-}P}}}{dt} \\ &= -\frac{\mu_0 \left|\dot{S}_P\right|}{4\pi} \cdot \left| \int_{L_{\mathrm{cell}}} \frac{1}{{x_{\text{cell-}P}}^3} \cdot \frac{\partial I_i}{\partial t} d\dot{l} \times \dot{x}_{\text{cell-}P} \right| \\ &= -\frac{\mu_0 \left|\dot{S}_P\right|}{4\pi} \cdot \left| \int_{L_{\mathrm{cell}}} \frac{j\omega}{{x_{\text{cell-}P}}^3} \cdot \frac{\omega^2 B_0 \left|\dot{S}_{\mathrm{cell}}\right|}{(\omega^2 - {\omega_i}^2) L_i} \right. \\ &\quad \left. \times e^{j\omega t_{T\text{-}P}} \cdot d\dot{l} \times \dot{x}_{\text{cell-}P} \right| \\ &= -j\frac{f^3 B_0 \left|\dot{S}_{\mathrm{cell}}\right|}{2\pi(f^2 - {f_i}^2) L_i} e^{j\omega t_{T\text{-}P}} \frac{\mu_0 \left|\dot{S}_{\mathrm{P}}\right|}{4\pi} \\ &\quad \cdot \left| \int_{L_{\mathrm{cell}}} \frac{1}{{x_{\text{cell-}P}}^3} \cdot d\dot{l} \times \dot{x}_{\text{cell-}P} \right|\end{aligned} \tag{6}$$

where $\dot{S}_P$ and $\dot{S}_{\mathrm{cell}}$ are the area elements of point *P* and the unit cell, respectively.

Point *P* could be considered as the representative of *Rx* coil. The coupling of original magnetic is weak at point P ($\boldsymbol{B}_{T\text{-}P}$) when the transfer distance is longer. However, $\boldsymbol{B}_{\text{cell-}P}$ can be generated by unit cell of PACs at point *P*, because the unit cell is affected by $\boldsymbol{B}_{T\text{-cell}}$. Consequently, $\boldsymbol{B}_{\text{cell-}P}$ is introduced to enhance the component of the incoming magnetic field at point *P* in the direction of $\boldsymbol{B}_{T\text{-}P}$, thereby boosting the induced voltage at point *P*.

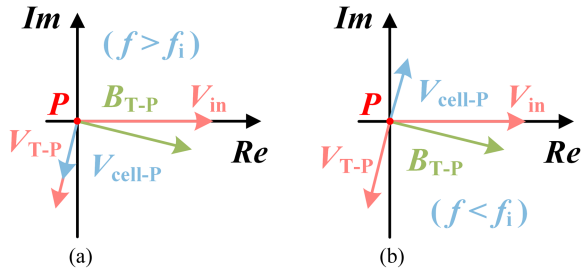

Fig. 4. Phase relationship between the induced voltage generated by the primary current and the current of a cell. (a) $f > f_i$. (b) $f < f_i$.

The phase relationship between $V_{\text{cell-}P}$ and $V_{T\text{-}P}$ at point *P* is shown in Fig. 4. Obviously, $V_{\text{cell-}P}$ and $V_{T\text{-}P}$ have the same direction when the resonant frequency of the unit cell is smaller than the operating frequency. Thus, the sum of induced voltages at point *P* increases. It means that the unit cell could increase the induced voltage and PTE of any point *P* of the magnetic coupling structure when $f_i < f$ and vice versa.

It should be noted that the relevant factors of the induced magnetic field of PACs are incompletely represented on (3), such as: the composition and position of the PACs. Therefore, we indirectly retrofit the transmission path of magnetic field by designing the impedance of PACs and the location of PACs to improve the transfer performance of the systems. In order to achieve the goal, we optimally design the length and width of the unit loop l_j, w_j [j = CACs parameters (cp) or AACs parameters (ap)], the number of turns n_{i} and the distance between PACs and *Tx* d_P while guaranteeing the relatively constant coupling strength between coils against lateral misalignment. Furthermore, the PTE of the WPT system can be achieved in (7) with the constraint of ZPA in primary side. The detailed analysis of the induced currents of each coil will be introduced in

Section III

$$\mathrm{PTE} = \frac{{I_R}^2 R_{\mathrm{eq}}}{U_{\mathrm{in}} I_{\mathrm{in}}}. \tag{7}$$

The following definitions apply to a WPT system with better misalignment tolerance: With the prerequisites of constant system inherent parameters (such as compensation capacitance, coil self-inductance, coil resistance, etc.), when *Rx* coil is shifted significantly, PTE changes slightly or remains constant. The calculation of PTE of the proposed WPT system would consume masses of computational resources, especially in the offset process. Hence, a new mathematic parameter, namely DF factor (DFF) is defined to raise the speed of calculation. It is used to evaluate the ability of misalignment tolerance of magnetic coupling structure with PACs based on equivalent mutual inductance $M_R'|_{\Delta y}$.

The PACs and *Tx* coil can be regarded as a black-box structure (*Tx'*), which can tactfully solve the complex mutual inductance in systems. The mutual magnetic flux between the *Tx'* and the *Rx* coil Ψ_{RT} is defined by (8). In addition, mutual magnetic flux Ψ_{RT} is described by (9) from the perspective of circuitry

$$\Psi_{RT} = N \cdot \int_{S_R} (\dot{B}_{T\text{-}R} + \dot{B}_{\mathrm{PACs}\text{-}R})\,|_{\Delta y} \cdot d\dot{S}_R \tag{8}$$

$$\Psi_{RT} = {M_R|_{\Delta y}}' \cdot i_{Tx} \tag{9}$$

where $d\dot{S}_R$ is the area elements of *Rx* coil, $\dot{B}_{T\text{-}R}$ and $\dot{B}_{\mathrm{PACs}\text{-}R}$ represent the magnetic flux density from the *Tx* coil and PACs to the area elements of the *Rx* coil, respectively. And i_{Tx} is the current of *Tx* coil.

Using (8) and (9), we could obtain the $M_R'|_{\Delta y}$ which is defined as the coupling between the *Tx'* structure and the *Rx* coil under the horizontal offset of the *Rx* coil

$${M_R|_{\Delta y}}' = \frac{N}{i_{\mathrm{T}}} \int_{S_R} (\dot{B}_{T\text{-}R} + \dot{B}_{\mathrm{PACs}\text{-}R})\,|_{\Delta y} \cdot d\dot{S}_R. \tag{10}$$

DFF could be expressed as

$$\mathrm{DFF} = \sqrt{\sum\nolimits_{\Delta y=0}^{x} \left({M_R|_{\Delta y}}' - {M_R|_{\Delta y=0}}'\right)^2} \Big/ {M_R|_{\Delta y=0}}' \tag{11}$$

where Δy denotes the horizontal offset distance of *Rx* coil's center. It is worth noted that the larger volume of PACs may reduce the practicability of the proposed WPT system. Additionally, it may lead to higher cost. Therefore, it is necessary to optimize the volume of PACs V_{PACs} while still ensuring higher PTE and better DF. The V_{PACs} is defined as (12). In order to gain the optimized results from multiple parameters, we build a mathematical model of a multi-objective optimization problem, and the prerequisite is to ensure higher PTE and better DF. The evaluation functions are shown as

$$V_{\mathrm{PACs}} = \left(12 \times \left({l_{cp}}^2 - (l_{cp} - 2 \cdot a \cdot n_{\mathrm{CACs}})\right)^2 + 4 \times \left({l_{ap}}^2 - (l_{ap} - 2 \cdot a \cdot n_{\mathrm{AACs}})^2\right) \cdot a \right. \tag{12}$$

$$\begin{cases} \text{Minimize DFF} = f_1(n_{\mathrm{CACs}}, l_{cp}, n_{\mathrm{AACs}}, l_{ap}, f_{\mathrm{CACs}}, f_{\mathrm{AACs}}, d_P) \\ \text{Minimize 1/PTE} = f_2(n_{\mathrm{CACs}}, l_{cp}, n_{\mathrm{AACs}}, l_{ap}, f_{\mathrm{CACs}}, f_{\mathrm{AACs}}, d_P) \\ \text{Minimize } V_{\mathrm{PACs}} = f_3\,(n_{\mathrm{CACs}}, l_{\mathrm{cp}}, n_{\mathrm{AACs}}, l_{ap}) \end{cases}. \tag{13}$$

According to (13), PTE, DFF and V_{PACs} are dependent on the various variables, such as resonant frequency of PACs, some structure parameters and distance. The optimization constraints of unit cell of PACs include turn number, the resonant frequency and unit coil size. In addition, PACs should not exceed a certain value and should be located in *Tx* coil and *Rx* coil. The restrictions that each parameter satisfies are illustrated in (14). Furthermore, to improve the DF of the proposed WPT system along different directions, the unit coil needs to satisfy $l_j = w_j$

$$\begin{cases} 1 \le n_{\mathrm{CACs}} \le 10, & 1 \le n_{\mathrm{AACs}} \le 10 \\ 60\ \mathrm{kHz} \le f_{\mathrm{CACs}} \le 110\ \mathrm{kHz}, & 60\ \mathrm{kHz} \le f_{\mathrm{AACs}} \le 110\ \mathrm{kHz} \\ 24\ \mathrm{mm} \le l_{cp} \le 120\ \mathrm{mm}, & 24\ \mathrm{mm} \le l_{ap} \le 120\ \mathrm{mm} \\ 0\ \mathrm{mm} \le d_P \le 400\ \mathrm{mm} \end{cases}. \tag{14}$$

The intervention of PACs changes the coupling relationship of the original WPT system, and the resonant relationship of the original compensation network is destroyed. It will affect the transfer characteristics of the WPT system. Therefore, the corresponding circuitry constraints are set: the voltage and current of *Tx/Rx* coil remain in phase. The circuitry constraints are listed in (15). It means that the WPT system with PACs has no reactive power. The specific derivation of the circuitry compensation network is described in Section III

$$\begin{cases} \cos\left\langle \dot{U}_{\mathrm{T}}, \dot{I}_{\mathrm{T}} \right\rangle = 1 \\ \cos\left\langle \dot{U}_{\mathrm{R}}, \dot{I}_{\mathrm{R}} \right\rangle = 1 \end{cases}. \tag{15}$$

The optimal design of PACs is an inverse electromagnetic field problem with multiple objective functions. Therefore, it is difficult to find the global optimal solution effectively by using traditional deterministic class search algorithms, such as GA, conjugate gradient method and direction acceleration method, and there is a lack of effective and reliable computing tools. Besides, nondominant sorting genetic algorithm (NSGA) and multiple objective particle swarm optimization have certain superiorities [20]: Optimization objectives are more numerous; noninferior optimal solutions are more evenly distributed; and multiple different equivalent solutions are allowed to exist. However, the large computational resources and lack of an elite strategy are unsuitable for the design of PACs. A comparison among the main features of the common optimization algorithms is shown in Fig. 5 [21], [22].

As an excellent algorithm for solving multiobjective optimization, NSGA-II can reduce computational complexity by introducing elite strategy. And it can ensure a uniform ranking of noninferior optimal solutions as well [23]. In spite of this, it is difficult to represent the characteristics of the solution space for traditional population initialization of NSGA-II due to the unknown concavity of the objective function. It could cause that optimization results are likely to fall into local optimal solutions and the global convergence of the algorithm is destroyed. In

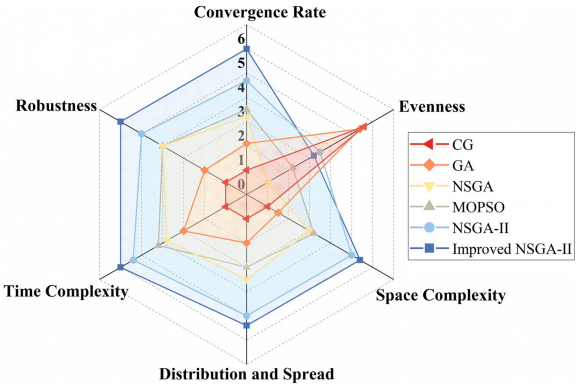

Fig. 5. Comparisons among the main features of the common optimization algorithms: conjugate gradient; genetic algorithm; NSGA; multiple objective particle swarm optimization; NSGA-II; and improved NSGA-II.

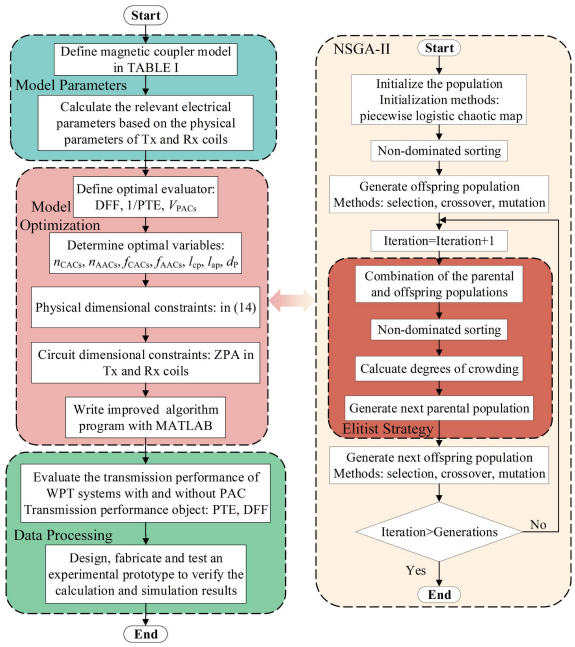

Fig. 6. Flowchart for optimizing the magnetic coupling structure.

order to solve this issue, the piecewise logistic chaotic map is proposed for population initialization. Although the improved NSGA-II occupies more computational resources, it can avoid the optimization results from being trapped in local optimum. And the optimization flowchart of magnetic coupling structure using improved NSGA-II is shown in Fig. 6.

The PTE as a function of DFF and V_{PACs} of the proposed magnetic coupling structure is shown in Fig. 7. In order to attain the optimal design, the PTE-DFF-$V_{\mathrm{PACs}}{}^*$ Pareto Front is plotted in Fig. 7. And each point (including the color) in Fig. 7 is a separate iterative individual. In fact, there is no one perfect point that simultaneously optimizes all objectives. Hence, it is necessary to determine the ideal point based on practical requirements (through principal component analysis), then the optimal parameters can be obtained. To facilitate analysis, this

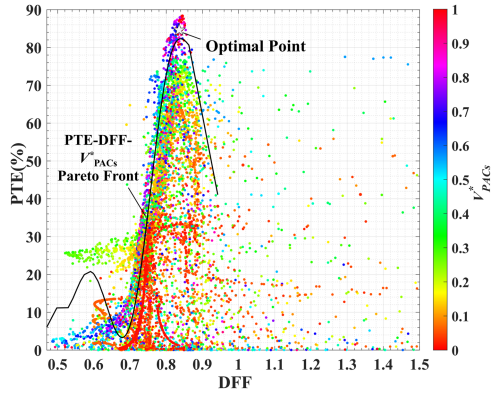

Fig. 7. Results of the magnetic coupling structure optimization.

TABLE II
COMPARISON OF PERFORMANCE BETWEEN ARBITRARY AND OPTIMIZED POINTS

	Point 1	Point 2	Point 3	Optimal point
PTE	85.5%	76.09%	81.5%	84.56%
DFF	0.8315	0.8477	0.8148	0.8242
V_{PACs}	237.2 cm^3	83.78 cm^3	245.6 cm^3	199.5 cm^3

article has formulated a weighted evaluation function by adopting min-max normalization, as listed in (16). Finally, the marked point with $n_{\mathrm{CACs}} = 8$, $n_{\mathrm{AACs}} = 4$, $l_{cp} = 120$ mm, $l_{ap} = 120$ mm, $f_{\mathrm{CACs}} = 75.7$ kHz, $f_{\mathrm{AACs}} = 60$ kHz, and $d_P = 255.5$ mm is chosen as the optimal design. In order to make the optimization process clearer, three optimization points are randomly selected in Pareto Front to compare the optimal design points, as given in Table II. It can be seen that that each of these points has its own advantages. However, the proposed optimization point has the strongest average strength

$$\begin{cases} S_{\mathrm{value}} = 0.6 \times \mathrm{PTE}^* - 0.3 \times \mathrm{DFF}^* - 0.1 \times V_{\mathrm{PACs}}{}^* \\ W_p{}^* = \frac{W_p - W_{p\min}}{W_{p\max} - W_{p\min}} \quad (W_p = \mathrm{PTE}, \mathrm{DFF or} V_{\mathrm{PACs}}) \end{cases} . \quad (16)$$

Based on the above variables, the incoming magnetic field generated by WPT system with PACs and without PACs are compared in the relatively large *XOY* plane where the *Rx* coil is located in Fig. 8. It should be observed that the operating conditions are that the input power is a certain constant, and that the circuit parts of the system have been impedance matched. It can be found that the addition of PACs enhances the incoming magnetic flux density at the plane of *Rx* coil and improve PTE of the system.

To further understand the mechanism of PACs to retrofit the transmitting magnetic field, we investigate the transmission path of transmitting magnetic field of the magnetic coupling structure with PACs and without PACs, as shown in Fig. 9. It becomes apparent that PACs can focus the transmitting magnetic field of the original magnetic coupling structure.

Lateral offsets of *Rx* coil along the *X*-axis or *Y*-axis have the same effect on transmission performance due to symmetrical magnetic coupling structure. Therefore, taking the *Y*-axis offset

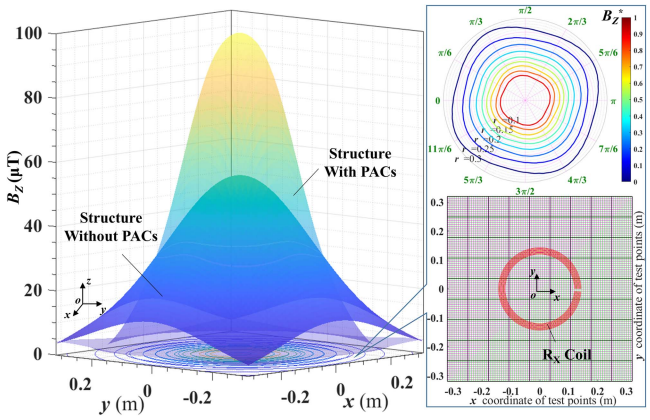

Fig. 8. Magnetic flux density distribution map of the WPT system with PACs and without PACs with invariant input power.

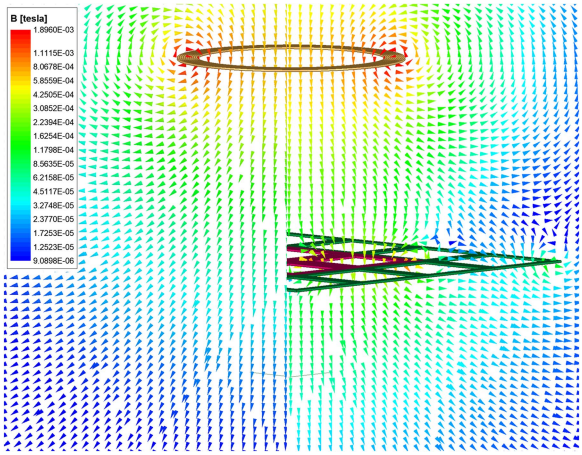

Fig. 9. Comparisons of the transmission path of transmitting magnetic field with PACs and without PACs.

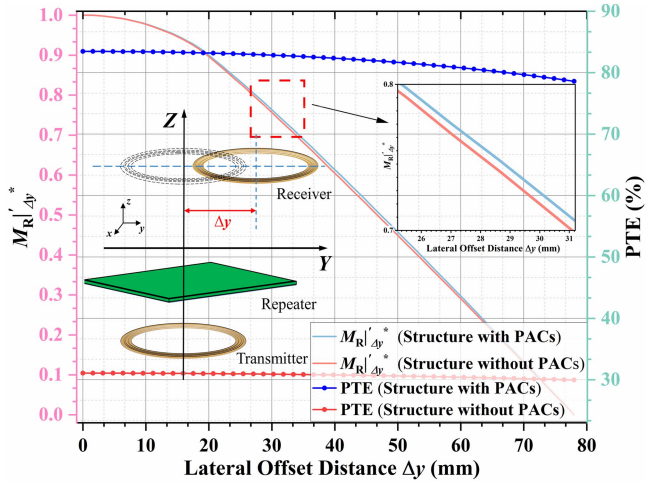

Fig. 10. Analysis and comparisons of lateral misalignment of $M_R{}'|_{\Delta y}{}^*$ and PTE for WPT system with PACs and without PACs.

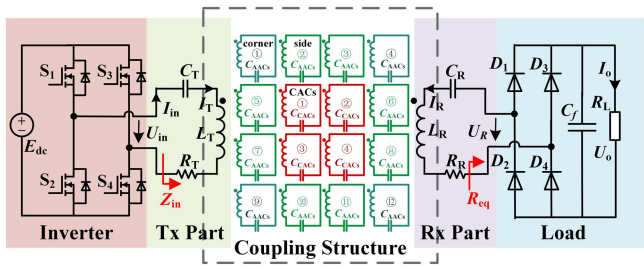

Fig. 11. Schematic circuit of the proposed WPT system.

as an example: the variation trend of PTEs and $M_R{}'|_{\Delta y}{}^*$ at misaligned conditions are shown in Fig. 10. $M_R{}'|_{\Delta y}{}^*$ is normalized by adopting min-max normalization. It can be observed that both PTE and $M_R{}'|_{\Delta y}$ of magnetic coupling structure with PACs are improved compared to the magnetic coupling structure without PACs. Therefore, the addition of PACs could improve PTE from 31.09% to 84.63% and decrease DFF by 66.51% of the WPT system.

III. Equivalent Circuit Analysis of WPT System

The circuit topology for the proposed WPT system with PACs is depicted in Fig. 11. The S-Ss-S compensation network is employed and represent that all resonators adopt SS topological compensation. This is because SS has great performance which is independent of the coupling coefficient and the load condition [24]. Each unit coil can be modeled with resistance, inductance and capacitance equivalently.

In order to achieve excellent electromagnetic modulation, the original field coupling condition is changed tactfully. Therefore, traditional compensation capacitor design methods are no longer applicable. A new parametric design method based on two-port theory is proposed. It ensures that ZPA could be realized in primary side. It is conductive to realize the efficient power conversion of the WPT system with PACs. Compared with conventional series compensation network, S-Ss-S could better adapt to the characteristics of the novel magnetic coupling structure, and improve the performance and stability of the WPT system with PACs.

It can be seen that the proposed WPT system includes five different kinds of loop: *Tx* coil; CACs; AACs (side, corner); and *Rx* coil. The impedance of different coils and the mutual inductance between coils of the same category in the PACs are expressed as (17) and (18), respectively. According to the KVL, a 5×5 voltage equation can be calculated as listed in (19), shown at the bottom of the next page. The AACs are divided into AAC side and AAC corner according to each group position. The calculated capacitance values can be gained flexibly by connecting the capacitors in series or parallel, which provides considerable freedom practical applications

$$\begin{cases} Z_{\mathrm{AACs}} = Z_{\mathrm{AACside}} = Z_{\mathrm{AACcorner}} \\ = j\omega C_{\mathrm{AACs}} + \dfrac{1}{j\omega L_{\mathrm{AACs}}} + R_{\mathrm{AACs}} \\ Z_{\mathrm{CACs}} = j\omega C_{\mathrm{CACs}} + \dfrac{1}{j\omega L_{\mathrm{CACs}}} + R_{\mathrm{CACs}} \\ Z_T = j\omega C_T + \dfrac{1}{j\omega L_T} + R_T \\ Z_R = j\omega C_R + \dfrac{1}{j\omega L_R} + R_R \end{cases} \tag{17}$$

TABLE III
MAIN ELECTRICAL PARAMETERS OF EXPERIMENTAL DEVICE WITHOUT PACS

Symbol	Value	Symbol	Value	Symbol	Value
L_T	53.2 μH	R_T	70 mΩ	C_T	65.9 nF
L_R	53.9 μH	R_R	70 mΩ	C_R	65.0 nF
	R_{eq}			10.2Ω	

TABLE IV
MAIN ELECTRICAL PARAMETERS OF EXPERIMENTAL DEVICE WITH PACS

Symbol	Value	Symbol	Value	Symbol	Value
L_T	53.2 μH	R_T	70 mΩ	C_T	62.6 nF
L_R	53.9 μH	R_R	70 mΩ	C_R	65.0 nF
L_{CACs}	12.1 μH	R_{CACs}	40 mΩ	C_{CACs}	365 nF
$L_{AACcorner}$	4.52 μH	$R_{AACcorner}$	14 mΩ	$C_{AACcorner}$	1.56 μF
$L_{AACside}$	4.50 μH	$R_{AACside}$	14 mΩ	$C_{AACside}$	1.557 μF
	R_{eq}			10.2Ω	

TABLE V
MAIN PHYSICAL PARAMETERS OF EXPERIMENTAL EQUIPMENT WITH PACS

Symbol	Value	Symbol	Value	Symbol	Value
h	400 mm	l_{cp}	120 mm	n_{CACs}	8
d_P	255.5 mm	l_{ap}	120 mm	n_{AACs}	4
w_{cp}	120 mm	w_{ap}	120 mm	d	240 mm
Litz Wire		Strand Number	300	Strand Diameter	0.1 mm

where Z_T and Z_R define the impedance of *Tx* coil and *Rx* coil at the operating frequency, respectively,

$$\begin{cases} X_{\text{corner}} = 2j\omega M_{\text{A1A4}} + j\omega M_{\text{A1A12}} \\ X_{\text{side}} = j\omega\Big(M_{\text{A2A3}} + M_{\text{A2A10}} + M_{\text{A2A5}} + 2M_{\text{A2A6}} \\ \qquad\qquad +M_{\text{A2A8}} + M_{\text{A2A11}}\Big) \\ X_{\text{CACs}} = 2j\omega M_{\text{C1C2}} + j\omega M_{\text{C1C4}} \end{cases} \tag{18}$$

where M_{AaCc} denotes the mutual inductance between the ath AACs and cth CACs.

where I_T and I_R are the currents of the *Tx* coil and *Rx* coil loops, respectively. I_{corner} and I_{side} are the currents of the AAC corner and AAC side coil loops, respectively.

M_a, M_b, and M_c satisfy

$$\begin{cases} M_a = 2\left(M_{\text{A1A2}} + M_{\text{A1A3}} + M_{\text{A2A4}} + M_{\text{A3A4}}\right) \\ M_b = M_{\text{A2C2}} + M_{\text{A2C3}} + M_{\text{A3C3}} \\ M_c = M_{\text{A1C2}} + M_{\text{A2C2}} + M_{\text{A1C3}} + M_{\text{A2C3}} \end{cases}. \tag{20}$$

Extract the second row to the fourth row in (19), and rewrite as block matrix, as shown in

$$\boldsymbol{O} = \begin{bmatrix} \boldsymbol{\alpha} & \boldsymbol{\chi} & \boldsymbol{\beta} \end{bmatrix} \begin{bmatrix} I_T \\ \boldsymbol{I_\chi} \\ I_R \end{bmatrix} \tag{21}$$

where

$$\begin{cases} \boldsymbol{\alpha} = \begin{bmatrix} 4j\omega M_{\text{tcorner}} \\ 8j\omega M_{\text{tside}} \\ 4j\omega M_{\text{tCACs}} \end{bmatrix}, \boldsymbol{\beta} = \begin{bmatrix} 4j\omega M_{\text{rcorner}} \\ 8j\omega M_{\text{rside}} \\ 4j\omega M_{r\text{CACs}} \end{bmatrix}, \\ \boldsymbol{I_\chi} = \begin{bmatrix} I_{\text{corner}} \\ I_{\text{side}} \\ I_{\text{CACs}} \end{bmatrix} \\ \boldsymbol{\chi} = \begin{bmatrix} 4(Z_{\text{AACs}} + X_{\text{corner}}) & 4j\omega M_a & 4j\omega M_b \\ 4j\omega M_a & 8(Z_{\text{AACs}} + X_{\text{side}}) & 8j\omega M_c \\ 4j\omega M_b & 8j\omega M_c & 4(Z_{\text{CACs}} + X_{\text{CACs}}) \end{bmatrix} \end{cases}. \tag{22}$$

Extract the first and last rows in (19) shown at the bottom of this page, and solve by associating with (21)

$$\begin{bmatrix} U_{\text{in}} \\ 0 \end{bmatrix} = \begin{bmatrix} Z_{\text{T}} & \boldsymbol{\alpha}^T & j\omega M_{tr} \\ j\omega M_{tr} & \boldsymbol{\beta}^T & Z_R + R_{\text{eq}} \end{bmatrix} \begin{bmatrix} I_T \\ \boldsymbol{I}_\chi \\ I_R \end{bmatrix}. \tag{23}$$

Using and simplifying (21)–(23), we derived the input impedance of two-port network Z_{in}

$$Z_{\text{in}} = \frac{U_{\text{in}}}{I_{\text{in}}} = \frac{\left(Z_T - \boldsymbol{\alpha}^{\boldsymbol{H}}\boldsymbol{\chi}^{-\mathbf{1}}\boldsymbol{\alpha}\right)\cdot\left(Z_R + R_{\text{eq}} - \boldsymbol{\beta}^{\boldsymbol{H}}\boldsymbol{\chi}^{-\mathbf{1}}\boldsymbol{\beta}\right) - \left(j\omega M_{\text{tr}} - \boldsymbol{\alpha}^{\boldsymbol{H}}\boldsymbol{\chi}^{-\mathbf{1}}\boldsymbol{\beta}\right)\cdot\left(j\omega M_{\text{tr}} - \boldsymbol{\beta}^{\boldsymbol{H}}\boldsymbol{\chi}^{-\mathbf{1}}\boldsymbol{\alpha}\right)}{\left(Z_R + R_{\text{eq}} - \boldsymbol{\beta}^{\boldsymbol{H}}\boldsymbol{\chi}^{-\mathbf{1}}\boldsymbol{\beta}\right)} \tag{24}$$

Z_{in} could be a real number by calculating the numerical solution of C_T. It means that U_{in} and I_{in} have no phase difference. The rest of the compensation parameters need to satisfy

$$\begin{cases} j\omega L_R + 1/(j\omega C_R) = 0 \\ j\omega_{\mathbf{CACs}} L_{\mathbf{CACs}} + 1/(j\omega_{\mathbf{CACs}} C_{\mathbf{CACs}}) = 0 \\ j\omega_{\mathbf{AACs}} L_{\mathbf{AACs}} + 1/(j\omega_{\mathbf{AAC}} C_{\mathbf{AACs}}) = 0 \end{cases}. \tag{25}$$

IV. EXPERIMENTAL VERIFICATION

An experimental prototype of the proposed magnetic coupling structure has been constructed, as shown in Fig. 12. The main electrical parameters of the proposed experimental device with PACs and without PACs are given in Tables III and IV, respectively. The specifications of Litz-wire for each coil and the rest of the physical parameters of the experimental equipment are given in Table V.

$$\begin{bmatrix} U_{\text{in}} \\ 0 \\ 0 \\ 0 \\ 0 \end{bmatrix} = \begin{bmatrix} Z_T & 4j\omega M_{\text{tcorner}} & 8j\omega M_{\text{tside}} & j\omega M_{\text{tCACs}} & j\omega M_{tr} \\ 4j\omega M_{\text{tcorner}} & 4(Z_{\text{AACs}} + X_{\text{corner}}) & 4j\omega M_a & 4j\omega M_{\text{b}} & 4j\omega M_{r\text{corner}} \\ 8j\omega M_{\text{tside}} & 4j\omega M_a & 8(Z_{\text{AACs}} + X_{\text{side}}) & 8j\omega M_{\text{c}} & 8j\omega M_{r\text{side}} \\ 4j\omega M_{\text{tCACs}} & 4j\omega M_b & 8j\omega M_c & 4(Z_{\text{CACs}} + X_{\text{CACs}}) & 4j\omega M_{r\text{CACs}} \\ j\omega M_{tr} & 4j\omega M_{\text{rcorner}} & 8j\omega M_{\text{rside}} & 4j\omega M_{\text{rCACs}} & Z_R + R_{\text{eq}} \end{bmatrix} \begin{bmatrix} I_T \\ I_{\text{corner}} \\ I_{\text{side}} \\ I_{\text{CACs}} \\ I_R \end{bmatrix} \tag{19}$$

TABLE VI
PERFORMANCES COMPARISON OF THE PROPOSED WPT SYSTEM WITH PREVIOUS WORKS

Ref.	Operating Frequency	Transfer Distance	Radius (Tx coil)	PTE	Weight	Lateral misalignment tolerance (relative change rate) / maximum lateral distance
Cho et al. [14]	6.78 MHz	150 mm	No mention	41.70%	No ferrite	No mention
Das et al. [15]	1.7 GHz	100 mm	50 mm (square)	17%	No ferrite	64% (PTE with 0-distance is 130mm) / 53 mm
Lee et al. [17]	60 kHz	200 mm	85 mm	68.46%	No ferrite	No mention
Hua and Hu [18]	105 kHz	51.1 mm	32 mm	-	No ferrite	No mention
Liu et al. [25]	13.56 MHz	60 mm	120 mm (square)	83.59%	No ferrite	16.1% (PTE) / 100 mm
Wang et al. [26]	800 kHz	20 mm	50 mm	40%	Ferrite	42% (Mutual inductance) / 50 mm
Mosammam and Mirsalim [27]	85 kHz	130 mm	240 mm	92%	Ferrite (5.2kg)	10% (PTE) / 200 mm
This paper	**85 kHz**	**400 mm**	**120 mm**	**84.60%**	**No ferrite**	**5.8% (PTE) / 80 mm**

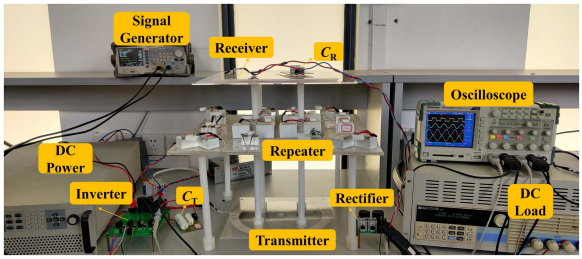

Fig. 12. Experimental device of the proposed WPT system.

To demonstrate the focusing effect of PACs, we measured the electromagnetic field strength of the WPT system with PACs and without PACs by using the spectrum analyzer RSA3030. It should be noted that the input power stays constant (50 W) when measuring the magnetic field, as shown in Fig. 13. The results show that the electromagnetic field strength of the proposed WPT system is improved by 22.17% at the center of the *Rx* coil. Therefore, the intervention of PACs can realize the focusing of the transmitting magnetic field in the Rx plane.

Simultaneously, the experimental waves are measured, as shown in Fig. 14. It can be observed that U_{in} and I_{in} have hardly phase difference after ignoring the fabrication errors. In addition, the waveforms associated with the WPT system without PACs are also measured under the condition of constant transmitting magnetic field. In parallel, the resonant frequency of magnetic structure without PACs is harmonized to 85 kHz for high power factor. And the waveforms are shown in Fig. 15. It can be seen that the proposed WPT system with PACs has higher PTE when *Rx* and *Tx* coils are placed coaxially.

The variation of PTE and output power of WPT system with PACs and without PACs with a certain lateral misalignment of *Rx* coil are depicted in Fig. 16. It could be found that the PTE of the proposed WPT system is increased by almost 50%. The relative variation rate of the efficacy relationship Δp (p = PTE or Output Power) is expressed as (26), where p and p_0 are the efficacy under the misalignment and alignment circumstance, respectively. Fig. 16(b) compares the Δp of the WPT system with PACs and without PACs at misaligned conditions. The

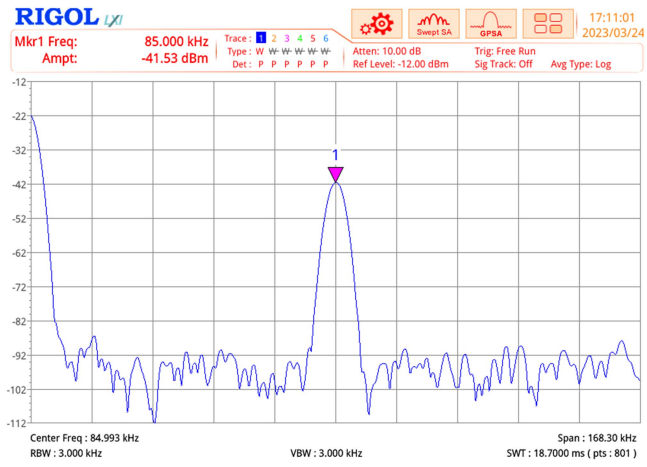

(a)

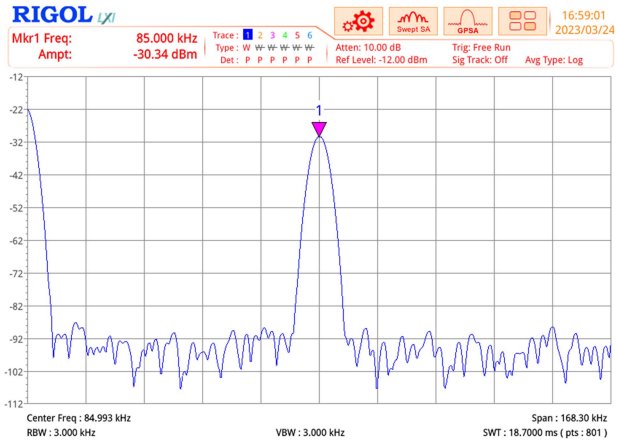

(b)

Fig. 13. Electromagnetic energy at the center of the *Rx* coil with invariant input power. (a) Magnetic coupling structure without PACs. (b) Magnetic coupling structure with PACs.

relative variation extent of both output power and PTE of the proposed WPT system are much lower than the original WPT system in the complete misalignment process. Especially, the maximum fluctuation rate of PTE and output power is 9% and

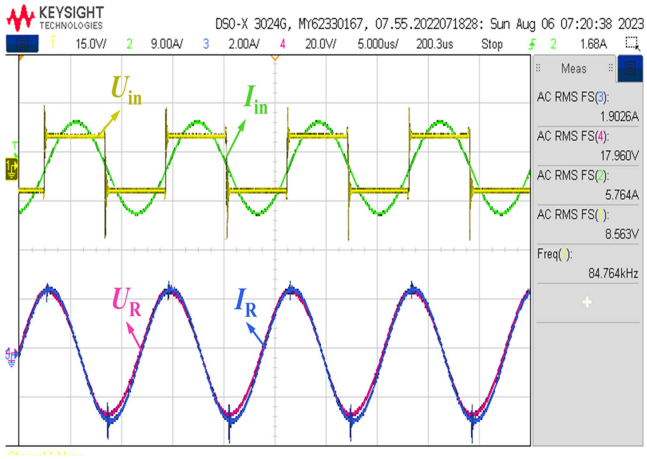

Fig. 14. Experimental waveforms of the proposed WPT system.

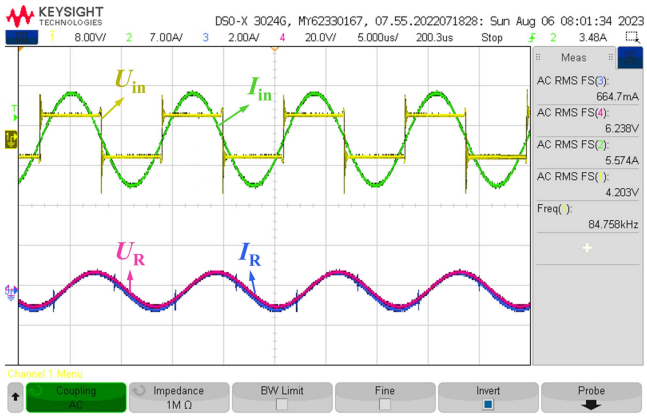

Fig. 15. Experimental waveforms of the WPT system without PACs.

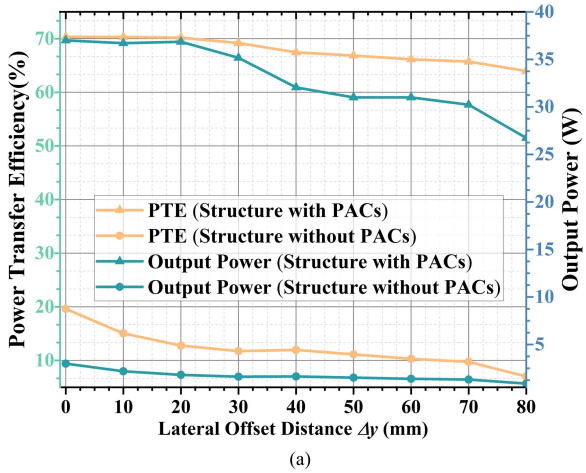

(a)

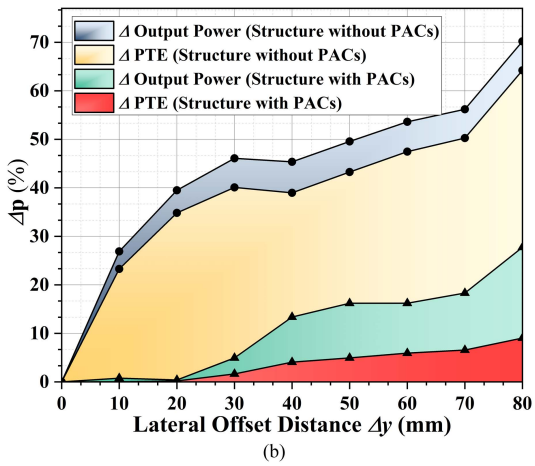

(b)

Fig. 16. Comparisons of lateral misalignment of PTE and output power for WPT system with PACs and without PACs. (a) Experimental results. (b) Relative variation rate.

27%, respectively,

$$\Delta p = \frac{p - p_0}{p_0} \times 100\%. \tag{26}$$

To verify the high performance of the proposed PACs, the article is compared with various other related studies. The transfer distance and the relative change rate of the corresponding evaluation factors (e.g., mutual inductance, PTE) had been given in Table VI. In the last column of Table VI, lateral misalignment tolerance indicates the relative change rate of the transfer performance of the WPT system under each known maximum offset condition, as listed in (26). Maximum lateral distance in Table VI represents the maximum offset condition. It can be observed obviously that the proposed WPT system has higher DF and PTE in the mid-range WPT system.

In summary, the comparison demonstrates that the magnetic coupling structure with PACs is not only favored in terms of PTE and misalignment tolerance improvement, but the proposed WPT system also provides longer transfer distance and lower weight.

V. Conclusion

A novel type of PACs is presented for high efficiency and good misalignment tolerance in the mid-range WPT system. To achieve this goal, the modified NSGA-II is put forward to optimize the parameters of magnetic coupling structure. The proposed PACs has the capability to effectively focus the leakage magnetic flux. Besides, a parameter design scheme for the compensation network named S-Ss-S topology is presented, which can increase the power factor of the WPT system with PACs. The simulation and experimental results show that the proposed WPT system could increase PTE by almost 50% and stabilize the PTE and output power (40 W) with lateral misalignment compared to the original WPT system. Hence, the proposed WPT system with PACs could provide useful guidance for various applications, such as IoTs, portable electronic devices, and smart home applications.

References

[1] S. Zhao, C. Xia, Z. Yang, H. Lu, H. Zhang, and C. Lu, "Bipolar checkerboard metal object detection without blind zone caused by excitation magnetic field for stationary EV wireless charging system," *IEEE Trans. Power Electron.*, vol. 38, no. 5, pp. 6696–6709, May 2023.

[2] Z. Zhang, H. Pang, A. Georgiadis, and C. Cecati, "Wireless power transfer—An overview," *IEEE Trans. Ind. Electron.*, vol. 66, no. 2, pp. 1044–1058, Feb. 2019.
[3] C. Rong et al., "A comprehensive analysis of metamaterial-coupled WPT systems for low electromagnetic field leakage," *IEEE Trans. Electromagn. Compat.*, vol. 65, no. 1, pp. 166–176, Feb. 2023.
[4] H. Wang, W. Wang, X. Chen, Q. Li, and Z. Zhang, "Analysis and design of kHz-metamaterial for wireless power transfer," *IEEE Trans. Magn.*, vol. 56, no. 8, Aug. 2020, Art. no. 6703215.
[5] R. Zhang et al., "Self-tuning WPT system with constant voltage output under resonance frequency shift," *IEEE Trans. Power Electron.*, vol. 39, no. 1, pp. 1713–1722, Jan. 2024.
[6] Y. Ma, Y. Sun, K. Cui, and X. Fan, "A 6.78-MHz digital rectifier-based single-stage wireless charger using digital-controlled CC–CV technique for implantable biomedical devices," *IEEE Trans. Power Electron.*, vol. 38, no. 1, pp. 101–106, Jan. 2023.
[7] M. J. Chabalko and A. P. Sample, "Resonant cavity mode enabled wireless power transfer," *Appl. Phys. Lett.*, vol. 105, no. 24, Dec. 2014, Art. no. 243902.
[8] Y. Chen, S. He, B. Yang, S. Chen, Z. He, and R. Mai, "Reconfigurable rectifier-based detuned series-series compensated IPT system for antimisalignment and efficiency improvement," *IEEE Trans. Power Electron.*, vol. 38, no. 2, pp. 2720–2729, Feb. 2023.
[9] M. Wang, G. Song, R. Yin, and Y. Shi, "Design and analysis of an antimisalignment wireless power transfer system," *IEEE Microw. Wireless Tech. Lett.*, vol. 33, no. 2, pp. 228–231, Feb. 2023.
[10] D. Brizi, N. Fontana, M. Tucci, S. Barmada, and A. Monorchio, "A spiral resonators passive array for inductive wireless power transfer applications with low exposure to near electric field," *IEEE Trans. Electromagn. Compat.*, vol. 62, no. 4, pp. 1312–1322, Aug. 2020.
[11] Z. Luo, X. Wei, M. G. S. Pearce, and G. A. Covic, "Multiobjective optimization of inductive power transfer double-d pads for electric vehicles," *IEEE Trans. Power Electron.*, vol. 36, no. 5, pp. 5135–5146, May 2021.
[12] B. M. Mosammam and M. Mirsalim, "New integrated tripolar pad using double-sided LCC compensation for wireless power transfer," *IEEE Trans. Veh. Technol.*, vol. 69, no. 12, pp. 15633–15643, Dec. 2020.
[13] S. Huh et al., "Transmitter coils selection method for wireless power transfer system with multiple transmitter coils and single receiver coil," *IEEE Trans. Power Electron.*, vol. 38, no. 3, pp. 4092–4109, Mar. 2023.
[14] Y. Cho et al., "Thin hybrid metamaterial slab with negative and zero permeability for high efficiency and low electromagnetic field in wireless power transfer systems," *IEEE Trans. Electromagn. Compat.*, vol. 60, no. 4, pp. 1001–1009, Aug. 2018.
[15] R. Das, A. Basir, and H. Yoo, "A metamaterial-coupled wireless power transfer system based on cubic high-dielectric resonators," *IEEE Trans. Ind. Electron.*, vol. 66, no. 9, pp. 7397–7406, Sep. 2019.
[16] H. Wang, W. Wang, X. Chen, Q. Li, and Z. Zhang, "Analysis and design of kHz-metamaterial for wireless power transfer," *IEEE Trans. Magn.*, vol. 56, no. 8, Aug. 2020, Art. no. 6703215.
[17] S. Lee et al., "Low leakage electromagnetic field level and high efficiency using a novel hybrid loop-array design for wireless high power transfer system," *IEEE Trans. Ind. Electron.*, vol. 66, no. 6, pp. 4356–4367, Jun. 2019.
[18] R. Hua and A. P. Hu, "Modeling and analysis of inductive power transfer system with passive matrix power repeater," *IEEE Trans. Ind. Electron.*, vol. 66, no. 6, pp. 4406–4413, Jun. 2019.
[19] *Wireless Power Transfer for Light-Duty Plug-In/Electric Vehicles and Alignment Methodology*, Standard SAE J2954, 2022.
[20] K. Deb, A. Pratap, S. Agarwal, and T. Meyarivan, "A fast and elitist multiobjective genetic algorithm: NSGA-II," *IEEE Trans. Evol. Comput.*, vol. 6, no. 2, pp. 182–197, Apr. 2002.
[21] X. Zhang, X. Zheng, R. Cheng, J. Qiu, and Y. Jin, "A competitive mechanism based multi-objective particle swarm optimizer with fast convergence," *Inf. Sci.*, vol. 427, pp. 63–76, Feb. 2018.
[22] C. Rong et al., "Optimization design of resonance coils with high misalignment tolerance for drone wireless charging based on genetic algorithm," *IEEE Trans. Ind. Appl.*, vol. 58, no. 1, pp. 1242–1253, Jan./Feb. 2022.
[23] Y. Zeng, C. Lu, R. Liu, X. He, C. Rong, and M. Liu, "Wireless power and data transfer system using multidirectional magnetic coupler for swarm AUVs," *IEEE Trans. Power Electron.*, vol. 38, no. 2, pp. 1440–1444, Feb. 2023.
[24] Z. Luo, X. Wei, M. G. S. Pearce, and G. A. Covic, "Multiobjective optimization of inductive power transfer double-D pads for electric vehicles," *IEEE Trans. Power Electron.*, vol. 36, no. 5, pp. 5135–5146, May 2021.
[25] Z. Liu et al., "A misalignment resilient system for magnetically coupled resonant wireless power transfer," *IEEE Trans. Antennas Propagat.*, vol. 68, no. 12, pp. 8260–8265, Dec. 2020.
[26] M. Wang, J. Feng, Y. Shi, and M. Shen, "Demagnetization weakening and magnetic field concentration with ferrite core characterization for efficient wireless power transfer," *IEEE Trans. Ind. Electron.*, vol. 66, no. 3, pp. 1842–1851, Mar. 2019.
[27] B. M. Mosammam and M. Mirsalim, "New integrated tripolar pad using double-sided LCC compensation for wireless power transfer," *IEEE Trans. Veh. Technol.*, vol. 69, no. 12, pp. 15633–15643, Dec. 2020.

Cancan Rong (Member, IEEE) was born in China in 1991. He received the Ph.D. degree in electrical engineering from the School of Electrical and Electronic Engineering, Huazhong University of Science and Technology, Wuhan, China, in 2021.

He is currently an Associate Professor with the China University of Mining and Technology, Xuzhou, China. His research interests include wireless power transfer system and metamaterials.

Mengmeng Chen received the B.Eng. degree in electrical engineering and automation in 2022 from China University of Mining and Technology, Xuzhou, China, where he is currently working toward the M.S. degree in electrical engineering with the School of Electrical Engineering.

His current research interests include the design and modeling of wireless power transfer with relay coils.

Xiaoyu Duan received the B.Eng. in electrical engineering and automation in 2022 from Henan Polytechnic University, Jiaozuo, China, where he is currently working toward the M.Eng. degree in electrical engineering with the School of Electrical Engineering, China University of Mining and Technology, Xuzhou, China.

His current research interests include the design and modeling of wireless power transfer with magnetic coupling and Unmanned Aerial Vehicles battery chargers.

Yunhai Liu was born in Shandong Province, China, in 1998. He received the B.S. degrees in electrical engineering from China University of Mining and Technology, Jiangsu, China, in 2021.

His research interests include wireless power transfer and intelligent control.

Junhao Wu received the B.Eng. in electrical engineering and automation in 2023 from China University of Mining and Technology, Xuzhou, China, where he is currently working toward the M.S. degree in electrical engineering with the School of Electrical Engineering, China University of Mining and Technology, Xuzhou, China.

His current research interests include the parity-time symmetric wireless power transfer and frequency bifurcation.

Yingqin Zeng was born in China in 1996. She received the B.E. degree in electrical engineering and automation from the Hebei University of Technology, Tianjin, China, in 2018. She is currently working toward the Ph.D. degree in electrical engineering with the School of Electrical and Electronic Engineering, Huazhong University of Science and Technology, Wuhan, China.

Her research interests include wireless power transfer system and metamaterials.

Xiangrui He was born in Jiangxi, China, in 1999. He received the B.E. degree of electrical engineering and automation in 2021 from Huazhong University of Science and Technology, where he is currently working toward the Ph.D. degree in electrical engineering from the State Key Laboratory of Advanced Electromagnetic Engineering and Technology Wuhan, China.

His current research interest is wireless power transfer and magnetic materials.

Zhijuan Liao received the B.S. and Ph.D. degrees in control theory and control engineering from the Chongqing University, Chongqing, China, in 2014 and 2019, respectively.

She is currently a Lecturer with the School of Electrical Engineering, China University of Mining and Technology, Xuzhou, Jiangsu, China. Her current research interests include wireless power transfer and power electronics.

Chenyang Xia (Member, IEEE) was born in Jiangsu Province, China, in 1982. He received the B.S., M.S., and Ph.D. degrees in control theory and control engineering from Chongqing University, Chongqing, China, in 2006, 2008, and 2010, respectively.

From 2018 to 2019, he was an Academic Visitor with the University of Auckland, Auckland, New Zealand. He is currently a Professor with the School of Electrical Engineering, China University of Mining and Technology, Xuzhou, China. His research interests include wireless power transfer and intelligent control.